DOI 10.24425/aee.2025.153913

Super-twisting sliding mode control strategy applied to a three-phase shunt active filter based on flying capacitor multicellular inverter

KHEIRA HEMICI^{®1}, MOHAND OULHADJ MAHMOUDI^{®1⊠}, ADIL YAHDOU^{®2}

¹Process Control Laboratory (PCL), National Polytechnic School BP. 182 El-Harrach, 16200 Algiers, Algeria ²University of Hassiba Ben Bouali 02000 Chlef, Algeria

e-mail: ⊠ mo.mahmoudi@g.enp.edu.dz, k.hemici@univ-chlef.dz, a.yahdou@gmail.com

(Received: 11.12.2024, revised: 14.08.2025)

Abstract: This paper introduces an innovative design for the super-twisting sliding mode control (ST-SMC) strategy, which is applied for the first time to a three-phase shunt active power filter (SAPF) utilizing a flying capacitor multicellular inverter (FCMI). The objective of the proposed ST-SMC is to enhance control over filter currents, flying capacitor voltages and the DC bus voltage. Simulation results, under balanced and unbalanced nonlinear load conditions, demonstrated exceptional capabilities in harmonic reduction while maintaining robust dynamic response characteristics. Additionally, it showed remarkable performance in tracking both filter currents, DC voltage, and flying capacitor voltages.

Key words: phase shifted pulse width modulation (PS-PWM), super-twisting sliding mode control (ST-SMC), three-phase flying capacitor multicellular inverter (FCMI), three-phase shunt active power filter (SAPF)

1. Introduction

The increasing use of nonlinear loads based on the power electronic elements introduced serious perturbation problems, such as harmonic pollution, current unbalance, and high consumption of reactive power [1]. To address these problems, the filters active and passive are connected to loads [2], one is the shunt active power filter (SAPF) [3], it efficiently eliminates load harmonics, ensuring that only the fundamental active current persists in the supply current, typically positioned at the point of common coupling (PCC).



© 2025. The Author(s). This is an open-access article distributed under the terms of the Creative Commons Attribution-NonCommercial-NoDerivatives License (CC BY-NC-ND 4.0, https://creativecommons.org/licenses/by-nc-nd/4.0/), which permits use, distribution, and reproduction in any medium, provided that the Article is properly cited, the use is non-commercial, and no modifications or adaptations are made. The first design was based on a two-level voltage source inverter (VSI) [4]. Multilevel inverters have been proposed to fulfill the demand for high-quality power [5]. Currently, three distinct multilevel inverter topologies are being explored: the diode-clamped multilevel inverter (DCMLI), the cascaded h-bridge inverter (CHBI), and the flying capacitor multilevel inverter (FCMLI).

Numerous papers in the literature compare these multilevel inverter topologies [6, 7]. The FCMLI exhibits several advantages [8], as it eliminates the need for stabilizing diodes, avoids issues related to DC link voltage imbalance, and allows for direct stabilization of the voltage across the switches. To improve the performance of the three-phase shunt active power filter (SAPF) based on the flying capacitor multicellular inverter (FCMI), various control algorithms have been explored in the literature [9–15].

The SAPF-FCMI is classified as a nonlinear multi-input multi-output (MIMO) system. Among the methods employed in the literature, the sliding mode control (SMC), is as a robust approach for nonlinear systems [16], characterized by its straightforward structure, ease of implementation, and robustness against disturbances. However, a notable drawback is the chattering phenomenon; various strategies for reducing chattering have been documented in the literature [17–20].

One method is high-order SMC, this control includes various control techniques. The supertwisting sliding mode control (ST-SMC) technique is the most prevalent. The super-twisting sliding mode control (ST-SMC) demonstrates superior performance compared to other control strategies across robustness, chattering reduction, and tracking precision. It is the most prevalent. Its main advantages include guaranteed stability and robustness.

The ST-SMC outperforms proportional-integral (PI) controllers in rejecting input disturbances. It reduces position-tracking error under noise, while PI shows error fluctuations. [21]. By comparison with conventional sliding mode control (SMC), the ST-SMC eliminates high-frequency oscillations (chattering) inherent in traditional SMC by using a continuous control law. This is critical for real-world applications like ball and beam balancers, where the ST-SMC reduces mechanical wear and energy consumption. The ST-SMC maintains robustness against uncertainties and disturbances while achieving smoother control inputs. For example, simulations on under actuated systems show that the ST-SMC reduces settling time by 30% compared to conventional SMC [22].

This study presents the development of super-twisting control applied to a shunt active power filter utilizing a flying capacitor multicellular inverter. The proposed control strategy ST-SMC aims to increase the stability of the SAPF-FCMI to handle load variations, which improves under conditions where efficiency and dynamic characteristics are maintained or even enhanced compared to conventional linear control methods based on a PI controller.

The paper is structured as follows: After an introduction to the subject, section 2 presents a description of the system and the mathematical model of the three-phase SAPF-FCMI, discussing the components represented in the system diagram. Section 3 introduces a control strategy for the SAPF-FCMI, emphasizing the application of the super-twisting sliding mode control (ST-SMC). Section 4 presents simulations that demonstrate the effectiveness of the proposed control strategy, evaluating the dynamic performance of the ST-SMC under unbalanced nonlinear load. Finally, Section 5 concludes with a summary of the main contributions of this work.

2. Description and principle of operation

2.1. Mathematical model

This section presents the topology of the three-phase SAPF-FCMI and its mathematical model in abc and dq phase coordinates. It also discusses the control strategies for the flying capacitor voltages and describes the algorithm used to generate the reference current.

Figure 1 illustrates the overall diagram of the three-level SAPF-FCMI, designed to mitigate harmonic currents and reactive power from the nonlinear load, represented in this study by a three-phase diode rectifier.

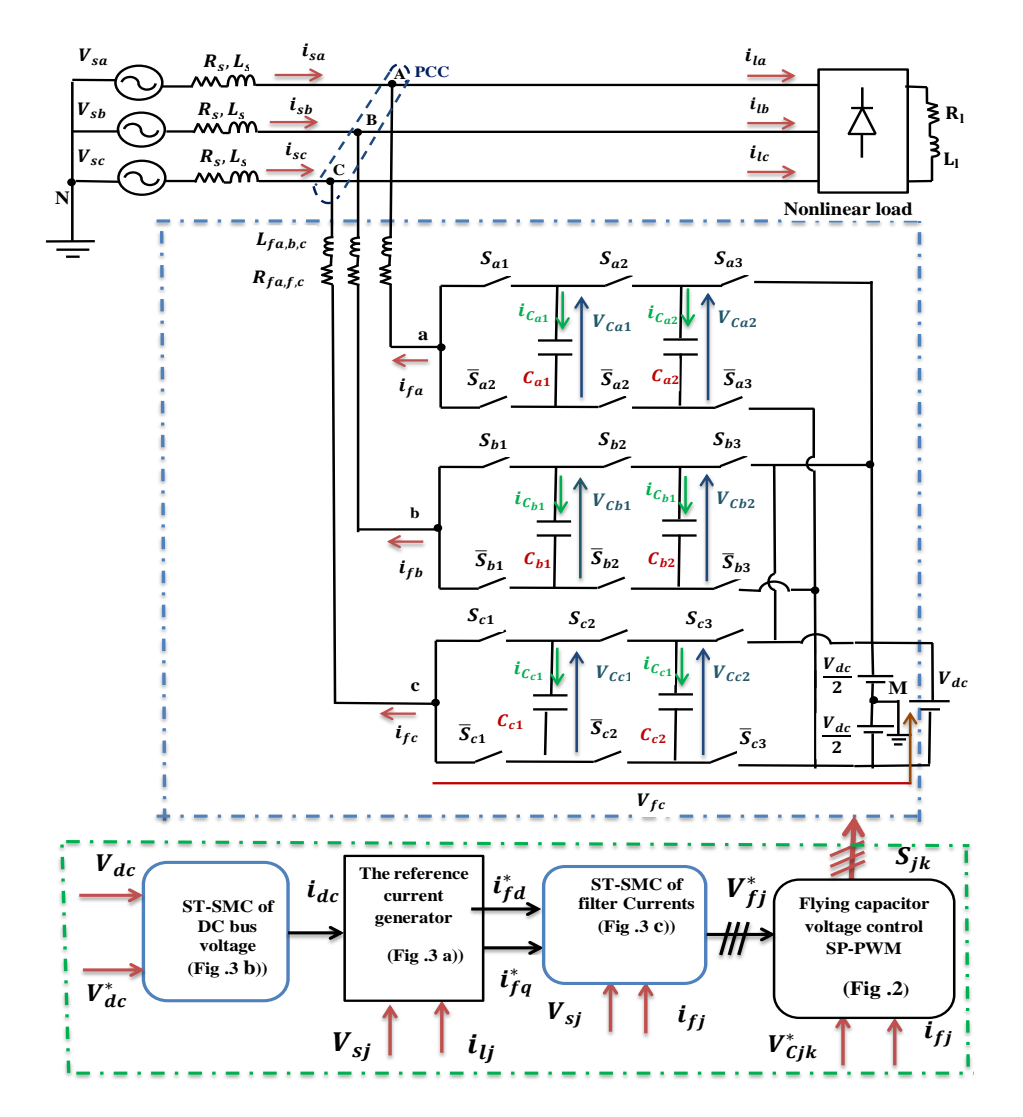


Fig. 1. Three-phase SAPF-FCMI system

The flying capacitor multicellular inverter (FCMI) utilizes two DC-bus capacitors to stabilize effectively the voltage. The SAPF-FCMI is connected to PCC distribution system via a coupling filter ($L_f R_f$). The differential equations describing the dynamic model of the three-phase SAPF-FCMI are defined in abc-axes, as given in Eq. (1) [23].

$$\begin{cases} L_{f} \frac{di_{fa}}{dt} = -R_{f}i_{fa} + v_{fa} - v_{sa} \\ L_{f} \frac{di_{fb}}{dt} = -R_{f}i_{fb} + v_{fb} - v_{sb} \\ L_{f} \frac{di_{fc}}{dt} = -R_{f}i_{fc} + v_{fc} - v_{sc} \\ \frac{dV_{dc}}{dt} = \frac{1}{C_{dc}}i_{dc}^{*} = \frac{P_{dc}^{*}}{C_{dc}V_{dc}} \end{cases}$$
(1)

The dynamical model of the system in dq reference frame results in Eq. (2) [24]:

$$\begin{cases}
\frac{\mathrm{d}i_{fd}}{\mathrm{d}t} = \frac{V_{fd}}{L_f} - \frac{R_f}{L_f} i_{fd} - \frac{V_{sd}}{L_f} - \omega i_{fq} \\
\frac{\mathrm{d}i_{fq}}{\mathrm{d}t} = \frac{V_{fq}}{L_f} - \frac{R_f}{L_f} i_{fq} - \frac{V_{sq}}{L_f} + \omega i_{fd}
\end{cases}$$
(2)

According to Eq. (2), the mathematical model of the proposed topology, three-phase SAPF-FCMI can expressed as:

$$\dot{x} = Ax + Bu + G. \tag{3}$$

Equation (3) presents the general state-space form, with:

$$x = \begin{bmatrix} i_{fd}, i_{fq} \end{bmatrix}^T$$
 State vector,

$$x = \begin{bmatrix} i_{fd}^*, i_{fq}^* \end{bmatrix}^T \text{ Reference vector,}$$

$$x^* = \begin{bmatrix} i_{fd}^*, i_{fq}^* \end{bmatrix}^T \text{ Reference vector,}$$

$$A = \begin{bmatrix} -\frac{R_f}{L_f} & -\omega \\ \omega & -\frac{R_f}{L_f} \end{bmatrix}, \quad B = \begin{bmatrix} \frac{1}{L_f} \\ \frac{1}{L_f} \end{bmatrix}, \quad u = \begin{bmatrix} V_{fd}, V_{fq} \end{bmatrix}^T \text{ Input vector,}$$

$$G = \begin{bmatrix} -\frac{V_{sd}}{L_f}, -\frac{V_{sq}}{L_f} \end{bmatrix}^T \text{ External perturbations to the system.}$$
The model grows stand in (2) describes the interaction between the active filt.

The model presented in (2) describes the interaction between the active filter connected to the PCC and the ac power system in (dq) coordinates, this mathematical model aids in identifying the control inputs, as well as the state and input variables. The model has two inverter currents (i_{fd}, i_{fq}) , the control inputs (V_{fd}, V_{fq}) are related to the control signal (s_{jk}) and the input voltages at the PCC (V_{sd}, V_{sq}) are treated as external perturbations to the system.

From system (2), the control inputs (V_{fd}, V_{fq}) are:

$$\begin{cases} V_{fd} = R_f i_{fd} + L_f \frac{\mathrm{d}i_{fd}}{\mathrm{d}t} + V_{sd} + L_f \omega i_{fq} \\ V_{fq} = L_f \frac{\mathrm{d}i_{fq}}{\mathrm{d}t} + R_f i_{fq} + V_{sq} - L_f \omega i_{fd} \end{cases}$$
 (4)

As shown in the equations of system (2), the filter currents (i_{fd}, i_{fq}) are coupled. To facilitate the regulation of these two components, it is necessary to decouple them. By introducing new

terms into the first and second equations of the system, we can express them as follows:

$$\begin{cases} u_d = R_f i_{fd} + L_f \frac{\mathrm{d}i_{fd}}{\mathrm{d}t} \\ u_q = L_f \frac{\mathrm{d}i_{fq}}{\mathrm{d}t} + R_f i_{fq} \end{cases} , \tag{5}$$

where

$$\begin{cases} V_{fd}^* = u_d + V_{sd} + L_f \omega i_{fq} \\ V_{fq}^* = u_q + V_{sq} - L_f \omega i_{fd} \end{cases} . \tag{6}$$

Equation (6) presents the control laws of the current loops.

As shown in Fig. 1, the blocks included in the three-phase SAPF-FCMI system are as follows:

- DC Link Voltage Control Block;
- Reference Current Generator Block;
- Current Injection Controller Block;
- Flying Capacitor Voltage Control Block.

The nonlinear load draws current that contains both harmonic and fundamental components. The role of the SAPF-FCMI is to produce harmonic currents of the same amplitude but opposite phase to counterbalance those absorbed by the load. This process aims to make the absorbed current sinusoidal within the network. Accurate detection of these harmonic currents is crucial. The SRF method is employed to generate reference signals for harmonic currents in the dq reference frame [26].

The mathematical representation of a given system is important when using the super-twisting algorithm (STA) because the relative degree of the model can be determined analytically, the STA is particularly suitable for implementation in systems of relative degree one [27].

2.2. Flying capacitor voltage control

In this study, we propose voltage-balancing dynamic in the FCMI using phase shifted-pulse width modulation (PS-PWM). We specialize in the three-cell inverter (p = 3) which represents a four-level FCMI, the control law balances the flying capacitor voltages to the defined values

$$V_{Cj1}^* = \frac{V_{dc}}{3}, \quad V_{Cj2}^* = \frac{2V_{dc}}{3}$$

and identifies the phase.

This makes the output voltage have four levels $\left\{0, \frac{V_{dc}}{3}, \frac{2V_{dc}}{3}, V_{dc}\right\}$.

The function of the switch is defined as (s_{jk}) .

Referring to Fig. 1, the voltage across the capacitor terminals is associated with the filter current and is influenced by the control of the switches. The current through the capacitor can be represented by Eq. (7).

$$\begin{cases} i_{C_{j1}} = (s_{j2} - s_{j1})i_{fj} \\ i_{C_{j2}} = (s_{j3} - s_{j2})i_{fj} \end{cases}$$
 (7)

The currents in flying capacitor $(C_{ik} = C)$ can be expressed by Eq. (8) [5]:

$$\begin{cases} i_{C_{j1}} = \frac{1}{C} \frac{dV_{Cj1}}{dt} \\ i_{C_{j2}} = \frac{1}{C} \frac{dV_{Cj2}}{dt} \end{cases}$$
 (8)

From Eqs. (7) and (8), we can extract:

$$\begin{cases} \frac{dV_{Cj1}}{dt} = \frac{1}{C}(s_{j2} - s_{j1})i_{fj} \\ \frac{dV_{Cj2}}{dt} = \frac{1}{C}(s_{j3} - s_{j2})i_{fj} \end{cases}$$
 (9)

 (s_{ik}) switch states as binary variables $(s_{ik} \in \{0, 1\})$, meaning "1" and "0" indicate the switch is on and off, respectively. The switch pairs in each phase function in a complementary manner $(s_{j1}, \overline{s_{j1}}, s_{j2}, \overline{s_{j2}}, s_{j3}, \overline{s_{j3}}).$

The line-to-ground voltage (V_{Mj}) and the currents through the flying capacitors (i_{Cj1}, i_{Cj2}) can be written using Kirchhoff's laws as:

$$V_{Mj} = (s_{j1} - s_{j2}) V_{Cj1} + (s_{j2} - s_{j3}) V_{Cj2} + s_{j3} \frac{V_{dc}}{2} - \frac{V_{dc}}{2}.$$
 (10)

From the preceding equations, we deduce that the current flowing through a capacitor is governed by the control signals linked to two consecutive switches within a switching period. The local-average representation of the capacitor current in Eq. (8) can be expressed as:

$$\begin{cases}
\bar{i}_{Cj1} = (d_{j2} - d_{j1})\bar{i}_{fj} \\
\bar{i}_{Cj2} = (d_{j3} - d_{j2})\bar{i}_{fj}
\end{cases},$$
(11)

where $(\bar{i}_{Cj1}, \bar{i}_{Cj2})$ are the locally-averaged currents of the capacitor (d_{j3}, d_{j2}, d_{j1}) , and are the duty cycles of the switch s_{j1} , s_{j2} and s_{j3} respectively, in general, duty cycles are defined as $(d_{ik} \in [0,1]).$

In the special case filter current $(i_{fj} > 0)$ and according to Eq. (9) the increase in the duty cycle d_{jk} results in an increased local-average current through the capacitor, while the latter decreases if d_{jk} is increased [28].

If the voltage $(V_{C_{ik}})$ across the Flying Capacitors exceeds its reference value, a negative current should be supplied to this capacitor. Consequently, d_{jk} should be increased while (d_{jk+1}) should be decreased. Conversely, if the filter current is negative $(i_{fj} < 0)$ the duty cycles should be adjusted in the opposite direction, to assist in balancing the voltage across the Flying Capacitors.

The balancing dynamic of flying capacitors voltage $(V_{C_{i1}}, V_{C_{i2}})$ is based on the following set of sequential equations:

$$\begin{cases}
\bar{i}_{Cj1} = C \frac{d\overline{V}_{Cj1}}{dt} \\
\bar{i}_{Cj2} = C \frac{d\overline{V}_{Cj2}}{dt}
\end{cases}$$

$$\begin{cases}
\frac{d\overline{V}_{Cj1}}{dt} = \frac{1}{C}\bar{i}_{Cj1} \\
\frac{d\overline{V}_{Cj2}}{dt} = \frac{1}{C}\bar{i}_{Cj2}
\end{cases}$$
(12)

$$\begin{cases} \frac{dV_{Cj1}}{dt} = \frac{1}{C}\bar{i}_{Cj1} \\ \frac{d\overline{V}_{Cj2}}{dt} = \frac{1}{C}\bar{i}_{Cj2} \end{cases}$$
(13)

From (11) and (13), we can obtain:

$$\begin{cases}
\frac{d\overline{V}_{Cj1}}{dt} = \frac{1}{C} (d_{j2} - d_{j1}) \, \overline{i}_{fj} \\
\frac{d\overline{V}_{Cj2}}{dt} = \frac{1}{C} (d_{j3} - d_{j2}) \, \overline{i}_{fj}
\end{cases}, (14)$$

where

$$\begin{cases} d_{j1} = d_{mj} + \Delta d_{j1} \\ d_{j2} = d_{mj} + \Delta d_{j2} \\ d_{j3} = d_{mj} + \Delta d_{j3} \end{cases}$$
 (15)

Here, (d_{mj}) represents the initial duty cycle of the switches, ranging within the interval [0, 1]. It is proportionate to the reference signal of the flying capacitors voltage (V_{fj}^*) and can be expressed as follows:

$$d_{mj} = V_{fj}^*. (16)$$

Using (15) in (14), we get the following:

$$\begin{cases}
\frac{\Delta \overline{V}_{Cj1}}{\mathrm{d}t} = \frac{1}{C} \mathrm{sign} \left(i_{fj} \right) \left(\Delta d_{j1} - \Delta d_{j2} \right) k_p \\
\frac{\Delta \overline{V}_{Cj2}}{\mathrm{d}t} = \frac{1}{C} \mathrm{sign} \left(i_{fj} \right) \left(\Delta d_{j2} - \Delta d_{j3} \right) k_p
\end{cases}$$
(17)

 k_p is the proportional control gain.

(sign (i_{fj})) is the sign of the filter current, which is equal to 1 and -1 when (i_{fj}) is positive and negative, respectively.

We express the duty cycles by the proportional controller, as Eq. (18):

$$\begin{cases} \Delta d_{j1} = \text{sign} (i_{fj}) (e_{j0} - e_{j1}) k_p \\ \Delta d_{j2} = \text{sign} (i_{fj}) (e_{j1} - e_{j2}) k_p \\ \Delta d_{j3} = \text{sign} (i_{fj}) (e_{j2} - e_{j3}) k_p \end{cases}$$
(18)

where e_{i0} , e_{i1} , e_{i2} and e_{i3} are the errors in the flying capacitors' voltages.

$$e_{jk} = \Delta V_{Cjk} = V_{Cjk}^* - V_{Cjk}, \quad k = \{1, 2\}.$$

We find

$$\begin{cases} \Delta d_{j1} = \text{sign}(i_{fj})(-e_{j1})k_p \\ \Delta d_{j2} = \text{sign}(i_{fj})(e_{j1} - e_{j2})k_p \\ \Delta d_{j3} = \text{sign}(i_{fj})(e_{j2})k_p \end{cases}$$
(19)

Replacement Eqs. (19) and (16) in (15),

$$\begin{cases}
d_{j1} = V_{fj}^* + \operatorname{sign}(i_{fj}) e_{j1} k_p \\
d_{j2} = V_{fj}^* + \operatorname{sign}(i_{fj}) (e_{j1} - e_{j2}) k_p \\
d_{j3} = V_{fj}^* + \operatorname{sign}(i_{fj}) e_{j2} k_p
\end{cases}$$
(20)

Replacement e_{i0} , e_{i1} and e_{i2} in Eqs. (20),

$$\begin{cases} d_{j1} = V_{fj}^* + \operatorname{sign}(i_{fj}) \left(-\left(V_{Cj1}^* - V_{Cj1} \right) \right) k_p \\ d_{j2} = V_{fj}^* + \operatorname{sign}(i_{fj}) \left(\left(V_{Cj1}^* - V_{Cj1} \right) - \left(V_{Cj2}^* - V_{Cj2} \right) \right) k_p \\ d_{j3} = V_{fj}^* + \operatorname{sign}(i_{fj}) \left(V_{Cj2}^* - V_{Cj2} \right) k_p \end{cases}$$
 (21)

Equation (21) defines the balancing dynamic of the proposed voltage control and can be used to tune the controller gain parameter (k_p) to achieve a satisfactory converter performance. Replacement Eqs. (19) in (17),

$$\begin{cases} \frac{\Delta \overline{V}_{Cj1}}{\Delta t} = \frac{1}{C} |\bar{i}_{fj}| (2e_{j1} - e_{j2}) k_p \\ \frac{\Delta \overline{V}_{Cj2}}{\Delta t} = \frac{1}{C} |\bar{i}_{fj}| (2e_{j2} - e_{j1}) k_p \end{cases}$$
(22)

Equation (22) gives the proposed balancing dynamic of the flying capacitor voltage control and which is used to adjust the gain parameter of the controller (k_p) in order to achieve satisfactory performance for the FCMI.

In order to reduce in a specific time (Δt), we express this time with the relation ($\Delta t = K/f$), where (K) denotes an integer multiple of fundamental periods, and (f) stands for the fundamental frequency. From Eq. (19), we extract:

$$k_p = \frac{fC}{2K[\bar{i}_{fi}]}. (23)$$

The average value of $(|\bar{i}_{fj}|)$, computed over a fundamental period, is given by:

$$\left|\bar{i}_{fj}\right|_{\text{avg}} = \frac{2\sqrt{2}I_{fj\text{rms}}}{\pi},\tag{24}$$

where (I_{fjrms}) is the RMS value of the filter current. We can replace $|\bar{i}_{fj}|$ in (23), with $(|\bar{i}_{fj}|_{avg})$. Eq. (23) becomes:

$$k_p = \frac{\pi f C_{jk}}{4\sqrt{2}KI_{firms}}. (25)$$

Equation (22) provides an approximation of the parameter (K) necessary for achieving balance in Flying Capacitor voltages. The determination of the number of periods can be made arbitrarily, and in practical applications, it is not strictly confined to whole numbers. It's important to observe that a lower value for (K) enhances the dynamics of voltage balancing. Typically, the parameter (K) is ideally set to one [28].

According to this study, the voltage balancing method is then developed, as presented in Fig. 2. The command signals (s_{jk}) of the cell switches (S_{jk}) are formed through mathematical comparison between the reference signals (d_{jk}) and the triangular signals (P_{jk}) defined by Eq. (26) as follows:

$$P_{jk} = \frac{2}{\pi} \left[a \sin \left(\sin \left(2\pi f_d t \right) - \varphi_{jk} - \frac{\pi}{2} \right) \right]. \tag{26}$$

The angle (φ_{jk}) is the same for all (P_{jk}) signals and is given by:

$$\varphi_{jk} = (k-1)\frac{2\pi}{p}.\tag{27}$$

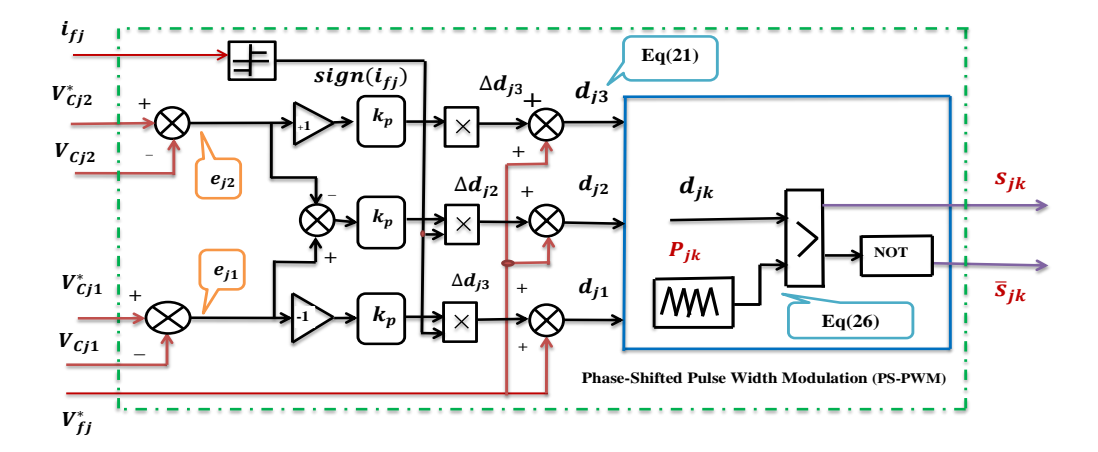


Fig. 2. Block diagram of the voltage balancing technique for four-level multicellular inverter using phaseshifted pulse width modulation (PS-PWM)

The control signal (s_{ik}) is determined as follows [29]:

$$s_{jk} = \left\{ \begin{array}{ll} 1 & \text{If reference signal } \geq P_{jk} \\ 0 & \text{Else} \end{array} \right..$$

As shown in Fig. 2, the three phase-shifted signal carriers (P_{jk}) are compared with the duty cycles of the switch (d_{jk}) , in order to generate switching pulses to drive the complementary switches $(S_{jk}, \overline{S}_{jk})$.

3. Proposed control design of SAPF-FCMI

Higher-order sliding mode algorithms have gained interest in reducing chattering effects, the super-twisting algorithm (STA), and an extension of a high-order sliding mode, has generated significant interest, and has become one of the most cited control techniques in the last two decades [30].

The ST-SMC achieves better trajectory tracking accuracy compared to conventional SMC or SO-SMC methods, it is suitable for diverse systems, including under actuated systems and nonlinear uncertain models. It is also characterized by simplified implementation without requiring derivatives, which makes it accessible for real-time applications. Guarantees global asymptotic stability with faster convergence rates, making it ideal for dynamic systems with high-performance demands [22–32].

Both the ST-SMC and SO-SMC are effective, their selection depends on the application, the ST-SMC is preferred for applications requiring smooth control signals and reduced computational complexity, such as motor drives or under-actuated systems. The SO-SMC excels in scenarios demanding high precision, robustness, and finite-time convergence, especially in systems with complex nonlinear dynamics, while the ST-SMC offers simplicity and smoothness in control actions. The SO-SMC provides superior robustness and precision at the expense of increased design complexity.

The super-twisting sliding mode control (ST-SMC) is a controller designed to eliminate the chattering effect, similar to second order sliding mode control (SO-SMC). However, the ST-SMC offers advantages over the SO-SMC by maintaining the same tracking performance and robustness [33]. The advantages of the ST-SMC include precision, good stability, simplicity, invariance, and robustness [19].

The stability criterion of the ST-SMC control is given by the Lyapunov stability approach, applied to sliding mode control [19, 20].

The super-twisting sliding mode control (ST-SMC) structure primarily consists of two components: equivalent control, which deals with the dynamics of the system and the sliding surface, and super-twisting-based switching control regarding the switching control, which is responsible for keeping the dynamics of the system onto the sliding surface. These components work synergistically to achieve robust trajectory tracking while mitigating chattering effects common in traditional sliding mode control.

The stability of the proposed control is ensured by the Lyapunov approach, which is expressed by the equation:

$$V(x) = \frac{1}{2}S^2(x). {(28)}$$

To ensure stability and convergence, the derivative of the Lyapunov function must be negative $(\dot{V}(x) = S\dot{S} < 0)$. The variable (x) can be the voltage (V_{dc}) or the filter currents (i_{fd}, i_{fq}) . The control law (u) of super twisting (ST) is constructed in two main parts. The first part is given by its derivative with respect to the time $(u_1(t))$. The second part is specified by the function of the sliding variable (u_1) [20].

Equation (29) represents the super-twisting algorithm:

$$\begin{cases} u = u_1 + \lambda |S|^{\rho} \operatorname{sign}(S) \\ u_1 = \alpha \cdot \operatorname{sign}(S) \end{cases} , \tag{29}$$

where (S) is the surface, and (λ) and (α) are positive values.

In this section, the SAPF-FCMI control based on the ST-SMC strategy with the PS-PWM technique is developed. It is important to note that the purpose of this control is to ensure that the DC voltage (V_{dc}) , the flying capacitor voltages (V_{Cj1}, V_{Cj2}) and filter currents (i_{fd}, i_{fq}) track their respective references.

3.1. Control the DC voltage (V_{dc})

To control the DC voltage (V_{dc}) , we apply a second order sliding mode (super-twisting) controller. The error vector is expressed as:

$$e_v = x_v^* - x_v = V_{dc}^* - V_{dc}. (30)$$

 e_v is the error in the DC voltage (V_{dc}) as shown in Eq. (31).

$$e_{v} = V_{dc}^{*} - V_{dc}. (31)$$

This error is considered to be the sliding surface of the sliding mode control [5], were V is the Lyapunov function.

The sliding mode surface (V_{dc}) is given by:

$$S_v = S(V_{dc}) = V_{dc}^* - V_{dc}.$$
 (32)

The Lyapunov function is expressed by Eq. (33):

$$V_{\nu} = \frac{1}{2} S_{\nu}^2. {33}$$

The deriving of the Lyapunov function is given in Eq. (34):

$$\dot{V}_{v} = S_{v} \cdot \dot{S}_{v}. \tag{34}$$

The deriving of sliding surface in the equation:

$$\dot{S}_{v} = \dot{V}_{dc}^{*} - \dot{V}_{dc}. \tag{35}$$

By replacing the expression of the derivative of the DC voltage V_{dc} (from Eq. (1)):

$$\dot{S}_{v} = \dot{V}_{dc}^{*} - \frac{1}{C_{dc}} i_{dc}^{*}. \tag{36}$$

Suppose an ideal sliding motion in [25]. This can be expressed as:

$$S_{\nu} = 0, \quad \dot{S}_{\nu} = 0.$$
 (37)

We can write the *first* derivative of the sliding surface in the following form:

$$\dot{S}_{v} = G_{v} - \frac{1}{C_{dc}} i_{dc}^{*} = u_{v}, \tag{38}$$

where $G_v = \dot{V}_{dc}^*$.

The second derivative of the sliding surface is given by:

$$\ddot{S}_{v} = \ddot{V}_{dc}^{*} - \frac{1}{C_{dc}} \dot{i}_{dc}^{*}. \tag{39}$$

Let's define the following inequality:

$$\begin{cases} \left| \dot{G}_{v} \right| \le C_{v} \\ 0 < K_{vm} \le \frac{1}{C_{dc}} \le K_{vM} \end{cases}$$
 (40)

If the sliding mode control stability criterion is applied [19, 20], the control of the DC voltage (V_{dc}) is given by Eq. (41):

$$\begin{cases} u_{\nu} = u_{1\nu} + \gamma |S_{\nu}|^{\rho} \operatorname{sign}(S_{\nu}) \\ \dot{u}_{1\nu} = \beta \cdot \operatorname{sign}(S_{\nu}) \end{cases}, \tag{41}$$

where

$$\beta > \frac{C_v}{K_{vm}}, \quad \gamma^2 \geq \frac{4C_v}{K_{vm}^2} \frac{K_{vM}(\beta + C_v)}{K_{vm}(\beta - C_v)}$$

and

$$0 \le \rho \le 1$$
.

 C_{v}, K_{vM}, K_{vm} are positive constants.

3.2. Control the filter currents (i_{fd}, i_{fq})

To control the filter currents (i_{fd}, i_{fq}) , we apply second order sliding mode (super-twisting) controller. The error vector is expressed as Eq. (42):

$$\begin{cases}
e_d = x_d^* - x_d = i_{fd}^* - i_{fd} \\
e_q = x_q^* - x_q = i_{fq}^* - i_{fq}
\end{cases}$$
(42)

This error is considered to be the sliding surface of the sliding mode control [5], where V is the Lyapunov function.

The sliding mode surface (S_d, S_q) is given by Eq. (43):

$$\begin{cases} S_d = S(i_{fd}) = i_{fd}^* - i_{fd} \\ S_q = S(i_{fq}) = i_{fq}^* - i_{fq} \end{cases}$$
 (43)

The stability of proposed control is assured by Lyapunov approach.

The Lyapunov function is expressed by Eq. (44):

$$\begin{cases} V_d = \frac{1}{2}S_d^2 \\ V_d = \frac{1}{2}S_q^2 \end{cases}$$
 (44)

The deriving of the Lyapunov function is given in Eq. (45):

$$\begin{cases} \dot{V}_d = S_d \cdot \dot{S}_d \\ \dot{V}_q = S_q \cdot \dot{S}_q \end{cases}$$
 (45)

The deriving of the sliding surface in Eq. (46):

$$\begin{cases} \dot{S}_{d} = \dot{i}_{fd}^{*} - i_{fd} \\ \dot{S}_{q} = \dot{i}_{fq}^{*} - i_{fq} \end{cases}$$
(46)

By replacing the expression of the derivative of the filter currents (i_{fd}, i_{fq}) (using Eq. (2)):

$$\begin{cases} \dot{S}_{d} = \dot{i}_{fd}^{*} - \frac{V_{fd}}{L_{f}} + \frac{V_{sd}}{L_{f}} + \omega i_{fq} + \frac{R_{f}}{L_{f}} i_{fd} \\ \dot{S}_{q} = \dot{i}_{fq}^{*} - \frac{V_{fq}}{L_{f}} + \frac{V_{sq}}{L_{f}} - \omega i_{fd} + \frac{R_{f}}{L_{f}} i_{fq} \end{cases}$$
(47)

Suppose an ideal sliding motion [23]. This can be expressed as Eq. (48):

$$\begin{cases}
S_d = 0, & \dot{S}_d = 0 \\
S_q = 0, & \dot{S}_q = 0
\end{cases}$$
(48)

We can write the first derivative of the sliding surface in the following form:

$$\begin{cases} \dot{S}_d = G_d + \frac{R_f}{L_f} i_{fd} \\ \dot{S}_q = G_q + \frac{R_f}{L_f} i_{fq} \end{cases}$$

$$\tag{49}$$

where

$$\begin{cases} G_{d} = i_{fd}^{*} - \frac{V_{fd}}{L_{f}} + \frac{V_{sd}}{L_{f}} + \omega i_{fq} \\ G_{q} = i_{fq}^{*} - \frac{V_{fq}}{L_{f}} + \frac{V_{sq}}{L_{f}} - \omega i_{fd} \end{cases}$$
(50)

The second derivative of the sliding surface is given by Eq. (51):

$$\begin{cases} \ddot{S}_d = \dot{G}_d + \frac{R_f}{L_f} \dot{i}_{fd} \\ \ddot{S}_q = \dot{G}_q + \frac{R_f}{L_f} \dot{i}_{fq} \end{cases}$$
 (51)

Let's define the following inequality:

If the sliding mode control stability criterion is applied [19, 20], the control of the currents filter (i_{fd}, i_{fg}) is given as shown in Eqs. (53):

$$\begin{cases} u_{d} = u_{1d} + \lambda |S_{d}|^{\rho} \operatorname{sign}(S_{d}) \\ \dot{u}_{1d} = \alpha \cdot \operatorname{sign}(S_{d}) \end{cases},$$

$$\begin{cases} u_{q} = u_{1q} + \lambda |S_{q}|^{\rho} \operatorname{sign}(S_{q}) \\ \dot{u}_{1q} = \alpha \cdot \operatorname{sign}(S_{q}) \end{cases},$$
(53)

where

$$\alpha > \frac{C_{dq}}{K_m}, \quad \lambda^2 \geq \frac{4C_{dq}}{K_m^2} \frac{K_M(\alpha + C_{dq})}{K_m(\alpha - C_{dq})}$$

and

$$0 \le \rho \le 1$$
.

 (C_{dq}, K_M, K_m) are positive constants.

The control signals (u_{fd}, u_{fq}) , from the ST algorithm are used to generate the switching signals for the three-phase flying capacitor multicellular inverter (FCMI). This can be achieved using phase-shifted pulse width modulation (PS-PWM) techniques.

Figure 3 shows the proposed block diagram of the ST-SMC scheme applied in the SAPF-FCMI.

4. Simulation and interpretations

The objective of this work is to verify the efficiency of the proposed ST-SMC controller for the SAPF FCMI in compensating harmonics, reactive power, and improving the quality of electrical power. The nonlinear load is a three-phase diode rectifier, and the system has been implemented, validated and realized using the MATLAB/Simulink package.

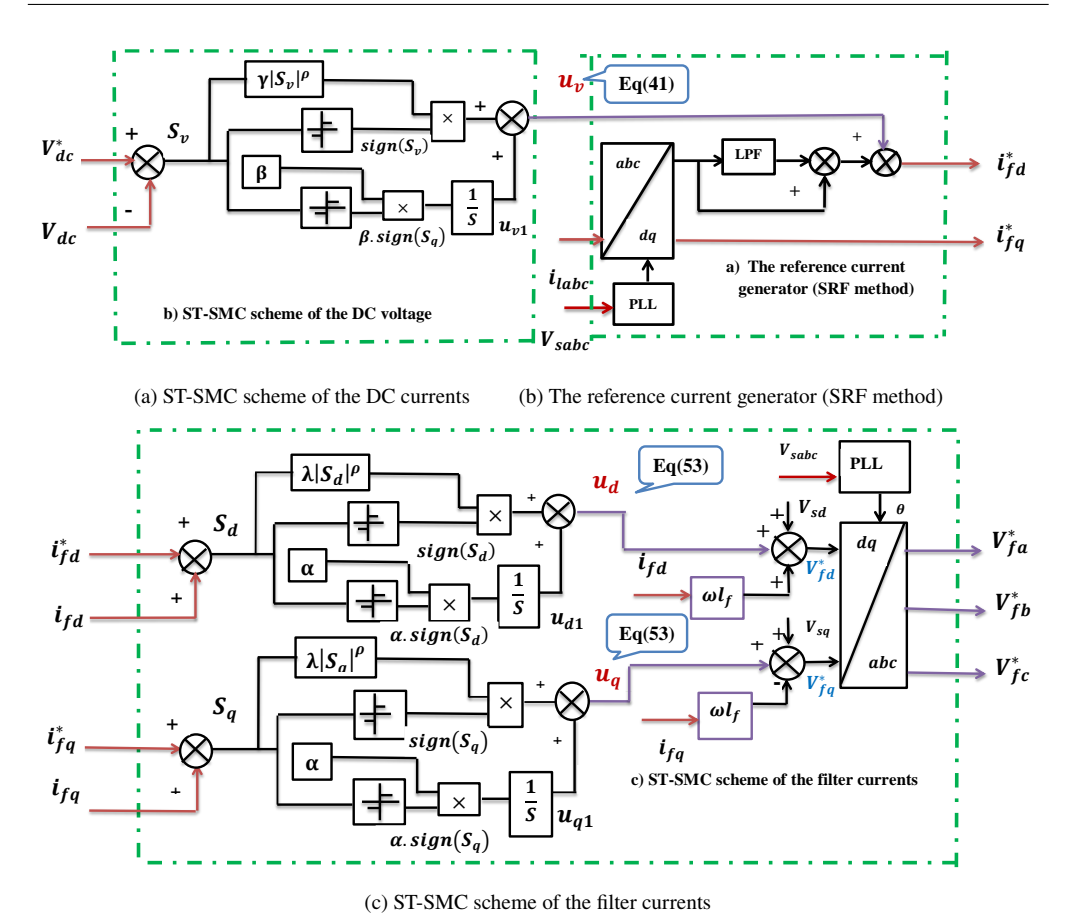


Fig. 3. Proposed block diagram of ST-SMC schema applied in SAPF-FCMI

The design of the system is based on Fig. 1 and Fig. 2. The SAPF measures the currents of the nonlinear load in real time. We use the SRF method to identify the reference filter currents (see Fig. 3(a)). The FCMI inverter is controlled by the phase-shifted pulse width modulation (PS-PWM) method to generate control signals for power semiconductors (Fig. 2). Using the ST-SMC, we compare the actual DC bus voltage with the reference voltage in order to achieve tight regulation of the DC bus voltage (Fig. 3(b)). We also use the ST-SMC to control the filter currents generated by the FCMI in order to force the actual filter current to track the reference compensation current as accurately and quickly as possible (Fig. 3(c)).

The system parameters used are based on reference [13] and are given in Table 1. The effectiveness of the SAPF-FCMI controlled by the ST-SMC, in terms of source currents, DC bus, and flying capacitor balancing, has been examined under unbalanced nonlinear load conditions. To demonstrate the good performance of the proposed controller during a transient, the non-linear load is increased at t = 0.6 s by adding another RL load in parallel to each existing load, effectively reducing the nonlinear load by 50%. The simulation results were compared to those obtained with a PI controller.

Table 1. Parameters	values	of the	simulated	l system	[13]
---------------------	--------	--------	-----------	----------	------

Parameter name	Symbol	Value	Unit
Source voltage	V_{sj}	220	V
Source frequency	f	50	Hz
Source impedance	R_S, L_S	1, 1	mΩ, mH
Load impedance	R_l, L_l	10, 10	Ω, mH
Coupling filter	R_f, L_f	1, 1	mΩ, mH
Capacitor in FCMI	C_{jk}	0.1	mF
DC Bus capacitance	C_{dc}	3	mF
DC bus voltage	V_{dc}	800	V
P-S PWM frequency	f_d	10	kHz
RMS value of the filter current	$I_{fj\mathrm{rms}}$	49.5	A
Integer multiple of fundamental periods	K	10	
The reference voltages	$V_{dc}^*, V_{Cj2}^*, V_{Cj1}^*$	800, 266.66, 533.33	V
ST-SMC gains	$egin{array}{c} lpha,\lambda, ho \ eta,\gamma \end{array}$	500, 500, 0.5, 20, 20	

Figure 4 shows the current waveform of the source (for phase (a)) and its total harmonic distortion (THD) before filtering with load change at t = 0.6 s. It is a highly non-sinusoidal and distorted current.

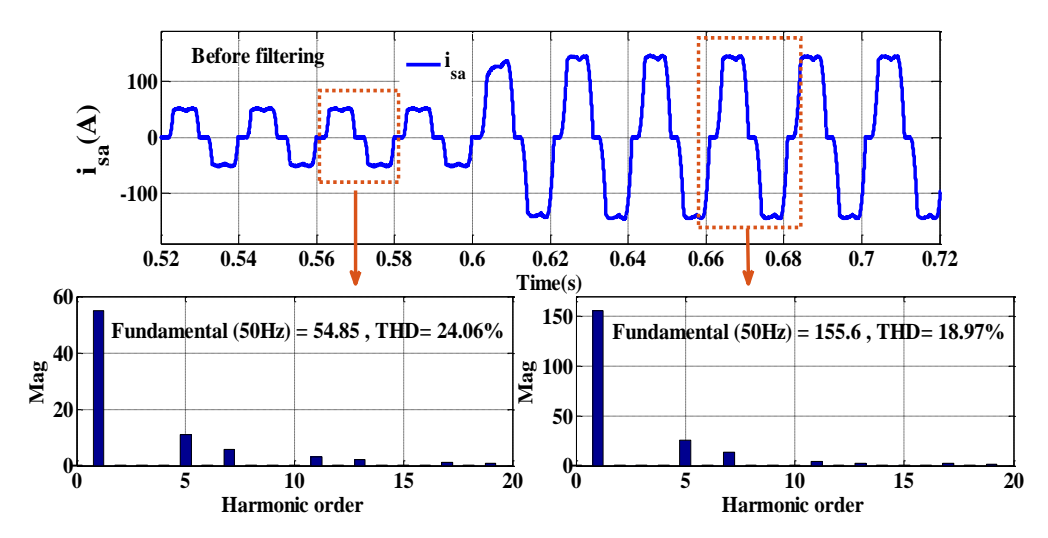


Fig. 4. Source current (i_{sa}) with THDs before SAPF-FCMI insertion and load change

After the insertion of the SAPF-FCMI and with the ST-SMC in operation, we test the efficiency and robustness of the ST-SMC control technique in terms of the stability of the DC voltage V_{dc} , flying capacitor voltages (V_{Cj1}, V_{Cj2}) , and filter currents (i_{fd}, i_{fq}) . We study the transient response, steady-state error, undershoot, and ripple voltage under unbalanced nonlinear load conditions.

To evaluate the performance of the SAPF-FCMI, we relied on several important metrics: transient response, steady-state error, and ripple voltage. The transient response is the time it takes for the SAPF-FCMI to react to changes in load conditions or disturbances in the power system. Steady-state error is the difference between the desired output $(V_{dc}^*, V_{Cj1}^*, V_{Cj2}^*, i_{fd}^*, i_{fq}^*)$ and the actual output $(V_{dc}, V_{Cj1}, V_{Cj2}, i_{fd}, i_{fq})$ of the filter once it has settled into a steady state. Ripple voltage refers to the voltage fluctuations of the DC voltage (V_{dc}) , flying capacitor voltages (V_{Cj1}, V_{Cj2}) and d-q filter currents (i_{fd}, i_{fq}) .

Figures 5, 6 and 7 show the response of (V_{dc}) and the flying capacitor voltages (V_{Cj1}, V_{Cj2}) . One can clearly observe that the dynamic performance of the ST-SMC is superior compared to PI control. The DC bus voltage regulation and the flying capacitor voltage regulation are achieved with a faster transient response time (0.15 s for ST-SMC, 0.32 s for PI) and a reduced ripple.

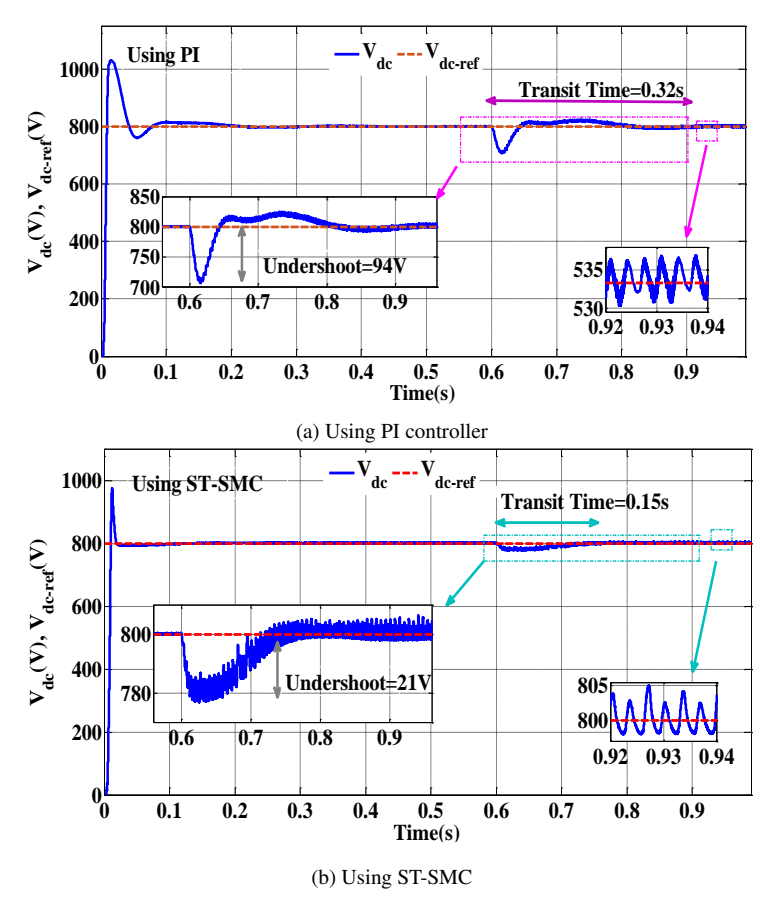


Fig. 5. DC bus voltage voltages V_{dc} under balanced and unbalanced nonlinear load

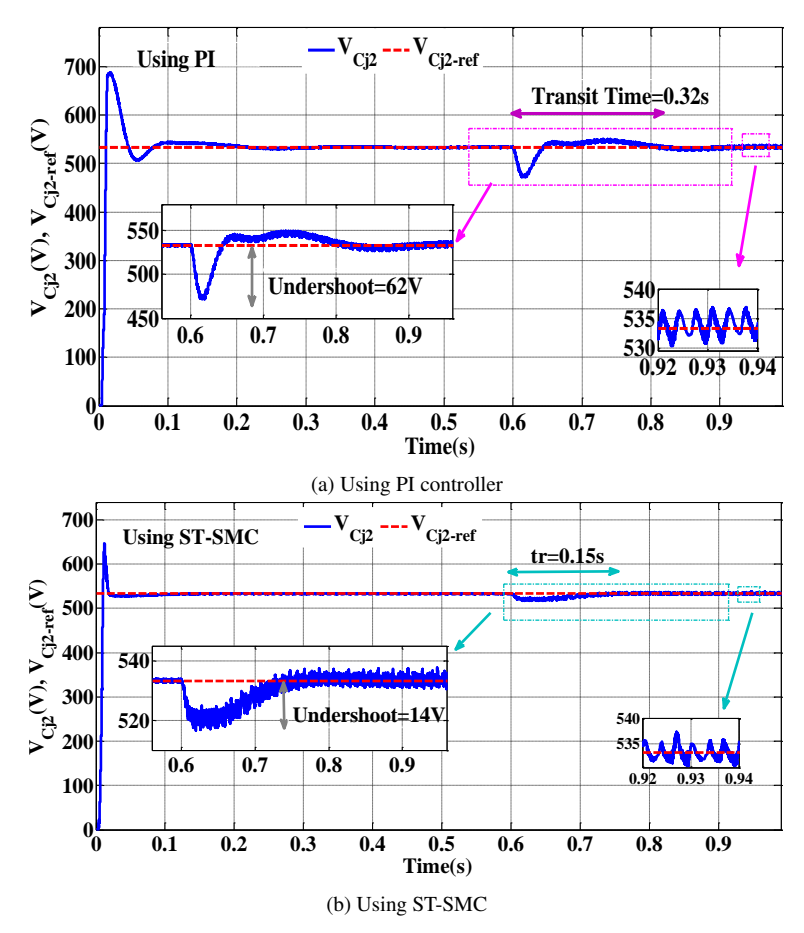
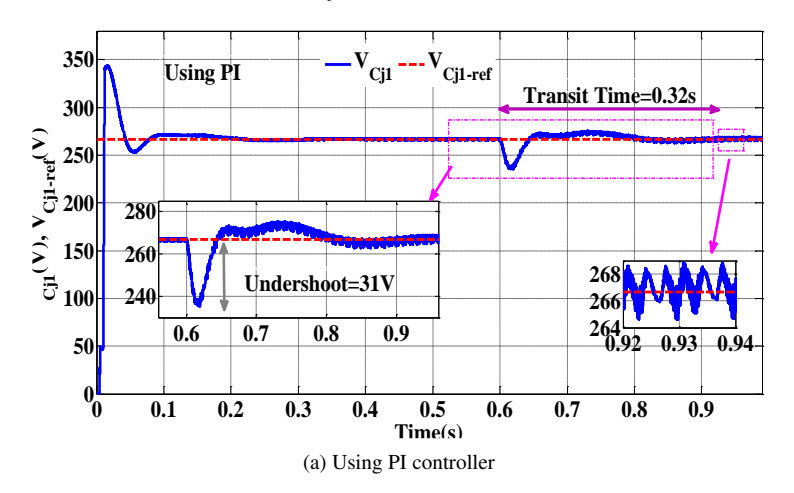


Fig. 6. Flying capacitor voltage V_{cj2} under balanced and unbalanced nonlinear load



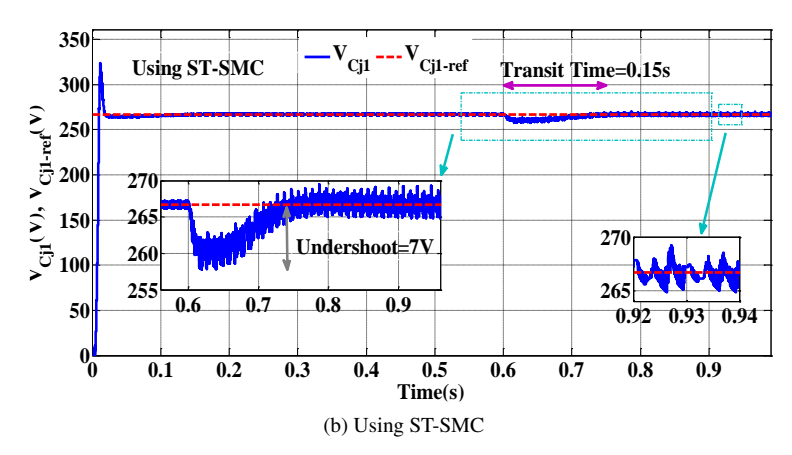


Fig. 7. Flying capacitor voltage V_{cj1} under balanced and unbalanced nonlinear load

With the ST-SMC controlled the SAPF-FCMI subjected to an unbalanced nonlinear load, the DC voltage V_{dc} and the flying capacitor voltages (V_{Cj1}, V_{Cj2}) exhibit maximum undershoots of 21 V, 14 V, and 7 V, respectively, which are estimated to be about 2.6% of their reference values. After a transient time of 0.15 s, each voltage aligns with its reference value (V_{dc}^*, V_{Cj1}^*) and V_{Cj2}^* , with a very small ripple estimated at 4 V. The steady-state error in these voltages is also very small compared to their reference values, as shown in Fig. 8.

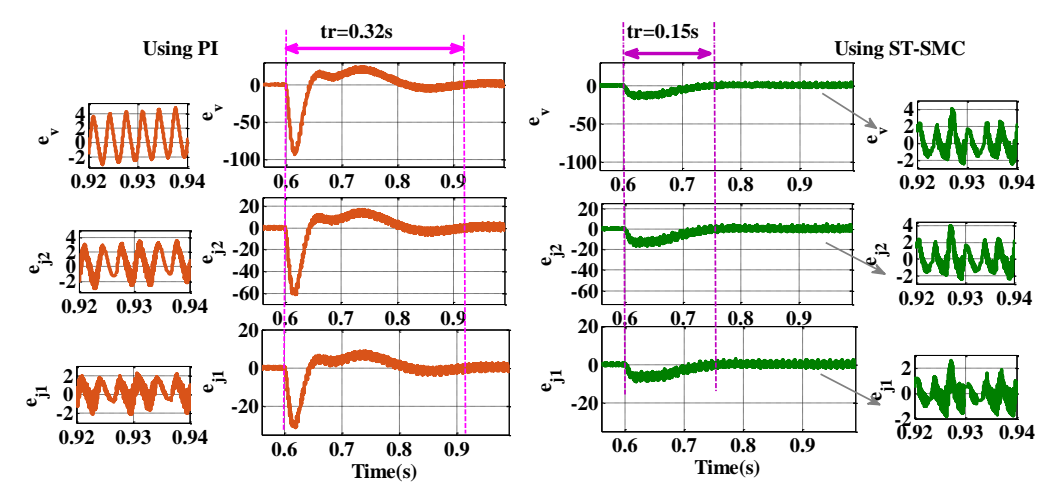


Fig. 8. Steady-state error for each of DC bus voltage and flying capacitor voltages

While we find that using PI the DC voltage and the flying capacitor voltages witness higher undershoots of (94 V, 62 V and 31 V), all estimated to be about 11.5% of the DC voltage and the flying capacitor voltages respectively, on the other hand, these voltages do not follow their reference values until after a transient time of 0.32 s.

Table 3 summarizes a comparison between the two control methods, with ST-MC we get a very small steady-state error compared to the conventional control PI; the transient response time of DC bus voltage and the flying capacitors voltages are reduced and estimated at 53.13% after an unbalanced nonlinear load. The recorded results effectively confirm the superiority of the suggested technique (ST-SMC).

Figure 8 shows a comparison of the performance of the two control strategies, PI and ST-SMC based on transit time and steady state error value after an unbalanced nonlinear load. By applying the ST-SMC, we got a short transit time (0.15 s) compared to transient response time by applying the PI controller (0.32 s). With the ST-SMC we get a very small steady state error and less transient response time compared to the conventional control PI, this allows the filter to compensate for disturbances and harmonics in real-time, resulting in greater efficiency in compensation of harmonic currents and reactive power; and improved power factor, thereby enhancing power quality and system stability.

Table 2. Performance comparison between ST-SMC and PI controllers in terms of the DC voltage and flying capacitor voltages

Voltage	Metric	Controller		
voitage	Wieu ic	ST-SMC PI		
	Undershoot (V)	7	94	
V_{dc}	Ripple voltage (V)	0.5	8	
	Steady-state error (V)	0.5	5	
	Transient response time (s)	0.15	0.32	
V_{Ci2}	Undershoot (V)	14	62	
	Ripple voltage (V)	4	6	
- 7-	Steady-state error (V)	3.8	4	
	Transient response time (s)	0.15	0.32	
V_{Cj1}	Undershoot (V)	7	31	
	Ripple voltage (V)	1	4	
	Steady-state error (V)	2	2	
	Transient response time (s)	0.15	0.32	

We conclude from this comparison that applying the **ST-SMC** ensures the stability of the DC voltage V_{dc} and the flying capacitor voltages (V_{Cj1}, V_{Cj2}) after a short transient response time. Therefore, it suffices to study the responses of the filter currents only by applying the **ST-SMC**. After the insertion of the **SAPF-FCMI**, the filter currents (i_{fd}, i_{fq}) follow their references within a short transient response time (tr), estimated at **0.04 s**, with a small steady-state error, as shown in Fig. 9 and Fig. 10 and summarized in Table 3.

With the **ST-SMC**, we can ensure that the actual filter current accurately and quickly tracks the reference compensation current. This enhances the effectiveness of the **SAPF-FCMI** in attenuating harmonics and/or reactive power. The results demonstrate that **lower ripple** and **low**

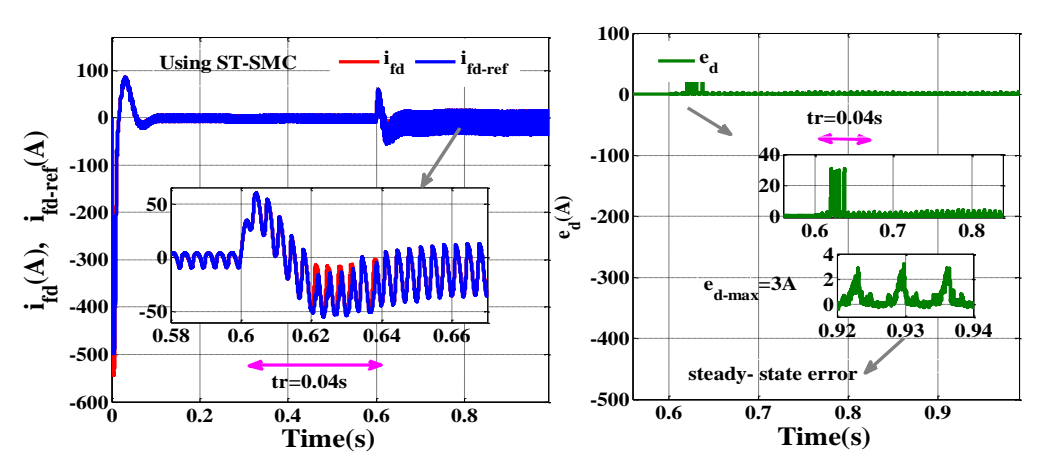


Fig. 9. Filter current (i_{fd}) and steady state error (e_d) under balanced and unbalanced nonlinear load

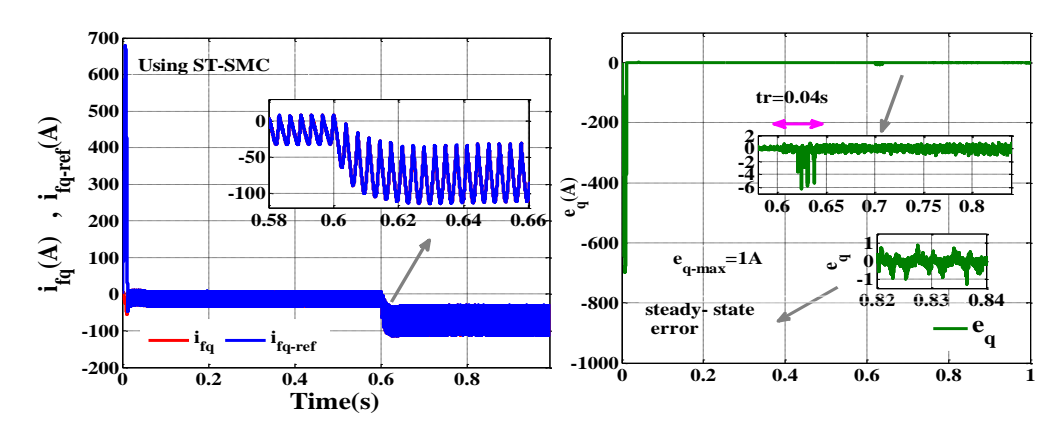


Fig. 10. Filter current (i_{fq}) and steady state error (e_q) under balanced and unbalanced nonlinear load

Table 3. The performance charac	eteristics using (ST-SMC	C) in terms of the filter	currents
---------------------------------	--------------------------	---------------------------	----------

	Metric	Symbol	t < 0.6 s	t > 0.6 s
<i>i</i>	Transient response time	tr (s)	0.1	0.04
i_{fd}	Steady-state error	$e_{d-\max}(V)$	3	3
i_{fq} –	Transient response time	tr (s)	0.1	0.04
	Steady-state error	$e_{q-\max}(V)$	0.5	1

overshoot indicate a more stable response, while a **short transient response time** suggests that the **SAPF-FCMI** can quickly return to a steady state. This improves its performance and reduces disturbances. Furthermore, a short transient response time leads to greater efficiency in attenuating harmonics and improving the power factor, which reduces energy losses and further enhances the performance of the **SAPF-FCMI**.

Based on the previous results, we can analyze the nature of the source current. Figures 11 and 12 demonstrate that after the insertion of the **SAPF-FCMI**, the **ST-SMC** achieves significantly lower THD values both before and after the load change (0.58% and 1.04%, respectively) compared to the results obtained with the **PI controller** (2.57% and 2.39%, respectively). This confirms that the **ST-SMC** is the most effective control strategy.

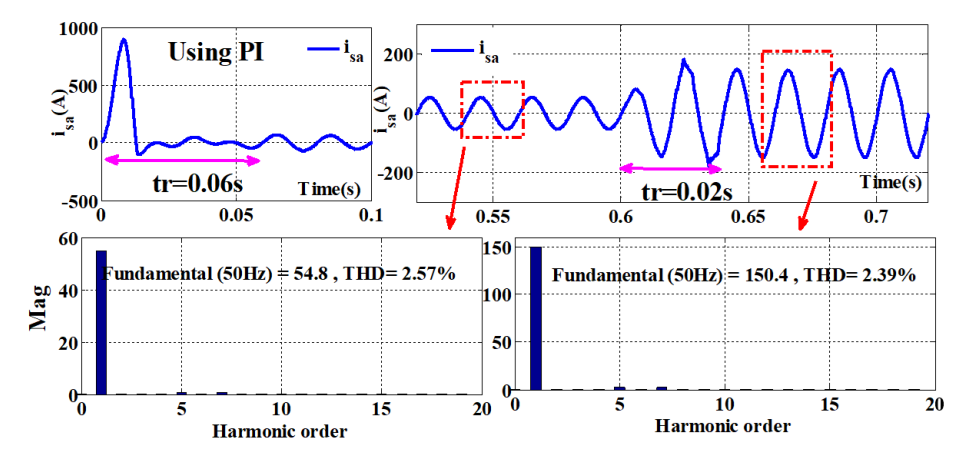


Fig. 11. Source current with THDs using the PI controller

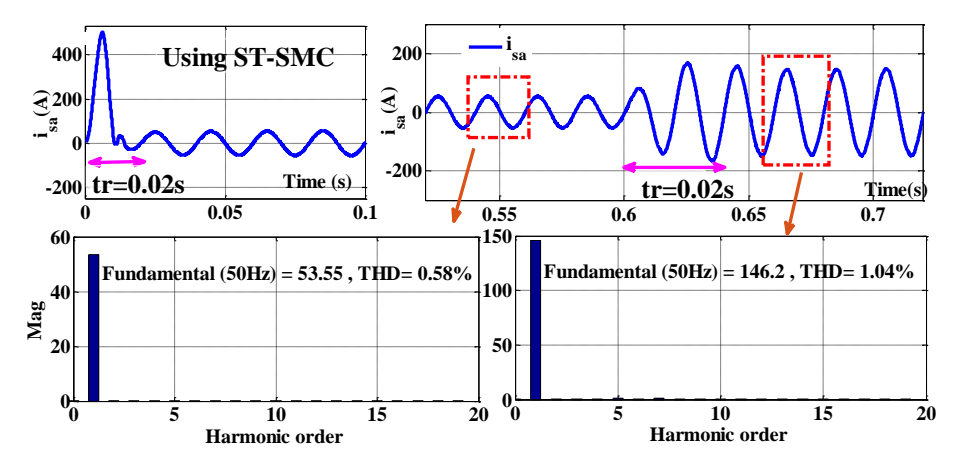


Fig. 12. Source current with THDs using the (ST-SMC)

The initial overshoot in the source current (Fig. 11 and Fig. 12) occurs during the transient phase when the SAPF-FCMI is activated. This is a typical response of dynamic control systems like the ST-SMC during abrupt load changes or filter engagement. The overshoot arises from the rapid adjustment of the control algorithm to compensate for harmonic currents and align the source current with the voltage phase.

	Symbol	t < 0.6	S	t > 0.6 s	
		ST-SMC	PI	ST-SMC	PI
Response time	tr	0.02	0.06	0.02	0.02
THD%	THD	0.58	2.57	1.04	2.39
RMS(A)	RMS	146.2	54.8	53.55	150.4
Overshoot	Ov	500	900	150	160

Table 4. The characteristics of source current SAPF-FCMI using ST-SMC and PI controller

Brief overshoots are unavoidable during transient periods. Despite the 0.02 s transient time, the total harmonic distortion (THD) remains low (0.58% before 0.6 s, 1.04% after), indicating no sustained harmonic distortion or system destabilization. If the overshoot magnitude exceeds component ratings (e.g., semiconductor devices), it could cause thermal stress. However, the robustness of the ST-SMC ensures transient overshoots are within safe limits.

Before the SAPF-FCMI operation, the source currents were highly distorted and rich in harmonics (Fig. 4). It is not in phase with the supply voltage, and this leads to the power factor being poor with high reactive power absorption.

When we connect the SAPF-FCMI controlled by the ST-SMC to the supply source, a filtering and composing process occurs, which makes the source currents sinusoidal and in phase with the supply voltages, as shown in detail in Fig. 13.

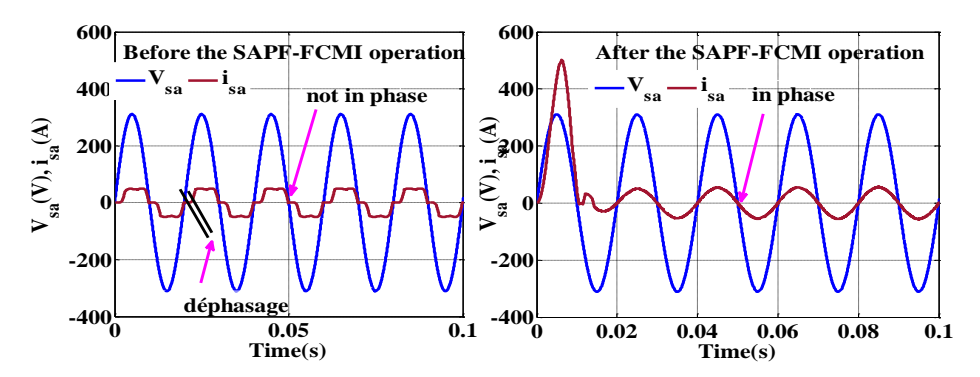


Fig. 13. Source current and source voltage before and after insertion of SAPF-FCMI

While both ST-SMC and PI control methods are capable of achieving sinusoidal source currents and phase alignment, there are notable differences in their performance characteristics. The ST-SMC approach offers superior robustness against parameter variations and external disturbances, making it ideal for dynamic and unpredictable operating conditions. Its ability to handle high-frequency switching noise also contributes to improved filtering accuracy.

On the other hand, PI control, while simpler to implement, may exhibit slower response times and reduced effectiveness under rapidly changing load conditions.

Figure 14 illustrates the performance of the system after the operation of the SAPF-FCMI, it compares between them in terms of the active power, reactive power, and power factor over time. Before the SAPF-FCMI operation, the active power and reactive power exhibit significant oscillations, indicating poor power quality. The power factor (PF) fluctuates significantly, staying below unity, which suggests inefficient deformed power resulting from harmonics.

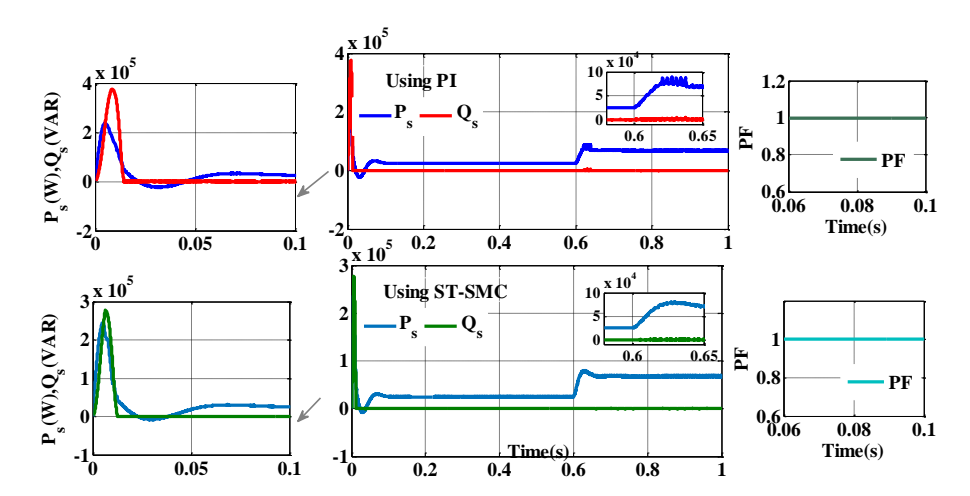


Fig. 14. Active and reactive power before and after insertion of SAPF-FCMI

After the SAPF-FCMI operation, the active power stabilizes after an initial transient response, showing improved filtering and compensation efficiency. The reactive power is significantly reduced, indicating effective compensation for reactive components. The power factor (PF) improves and approaches unity, demonstrating enhanced system performance and better alignment between voltage and current.

The active power (P_s) overshoot effects the sudden injection of compensating currents by the SAPF-FCMI to cancel load harmonics. This is linked to the transient energy exchange between the filter's DC-link capacitor and the grid, reactive power (Q_s) overshoot is the reactive power transient that occurs as the filter rapidly adjusts to achieve a unity power factor. Large overshoots could temporarily distort grid voltage, but the ST-SMC's fast settling time (0.02 s) minimizes this risk. Energy surges during transit time might strain the DC-link capacitor, but the ST-SMC mitigates this.

The increase in the magnitude of active and reactive power after connecting the filter could be due to the improved power factor and reduced harmonic distortion, which allows for more efficient power transfer. The SAPF-FCMI helps in compensating reactive power and harmonics, potentially increasing the effective active power. This increase can lead to more efficient energy utilization and reduced strain on the power distribution system.

However, it also means that the system's capacity to handle increased power demands should be assessed to avoid overloading. While overshoots can cause transient issues, the overall benefits of using the SAPF-FCMI for power quality improvement and power factor correction generally outweighs these concerns, provided the system stabilizes quickly and efficiently. The SAPF-CMI effectively improves power quality by reducing oscillations in the active power, minimizing the reactive power, and improving the PF as shown in Fig. 14.

5. Conclusion

In this study, a nonlinear method using the super-twisting sliding mode control (ST-SMC) with a phase shifted pulse width modulation (PS-PWM) technique is proposed to control a three-phase shunt active power filter based on a flying capacitor multicellular inverter. To highlight the performance of the suggested technique, the dynamic performance was tested under unbalanced nonlinear loads. Simulation results showed excellent performance using the super-twisting sliding mode control (ST-SMC) compared to the PI controller. This allows for a quicker retrieval to steady-state with minimal undershoot and ripple in both the DC voltage and flying capacitor voltages, demonstrating good robustness, low harmonic content, and effective reactive power compensation. The ST-SMC applied in the SAPF-FCMI offers increased robustness against unbalanced nonlinear loads. They can force the DC voltage, the flying capacitor voltages, and filter currents to follow their predefined paths in a finite time.

In conclusion, a comparison between the proposed PI and ST-SMC controllers highlighted the superiority of the ST-SMC approach. Moreover, compared to other published works, the ST-SMC technique gave much lower percentages of the THD value, it can be said that this technique effectively compensates the absorbed harmonic current, resulting in low reactive power consumption and unity power factor. Finally, the ST-SMC offers a robust and effective solution for controlling SAPF-FCMIs.

References

- [1] Kouzou A., Abu Rub H., Mahmoudi MO., Boucherit MS., Kennel R., *Four wire Shunt Active Power Filter based on four-leg inverter*, International Aegean Conference on Electrical Machines and Power Electronics and Electromotion, Istanbul, Turkey, vol. 8, no. 10, pp. 508–513 (2011), DOI: 10.1109/ACEMP.2011.6490651.
- [2] Hoon Y., Radzi M.A.M., Hassan M.K., Mailah N., Control Algorithms of Shunt Active Power Filter for Harmonics Mitigation, Energies, vol. 10, no. 12, 2038 (2017), DOI: 10.3390/en10122038.
- [3] Grugel P., Mucko J., Selected static characteristics of a parallel active power filter with feedback from the supply voltage, Archives of Electrical Engineering, vol. 73, no. 1, pp. 37–50 (2024), DOI: 10.24425/aee.2024.148855.
- [4] Thuyen C.M., *Adaptive current control method for hybrid active power filters*, Journal of Electrical Engineering, vol. 67, no. 5, pp. 343–350 (2016), DOI: 10.1515/jee-2016-0049.
- [5] Jafrodi S.T., Ghanbari M., Mahmoudian M., Najafi A., Rodrigues E.M.G., Pouresmaeil E., A Novel Control Strategy to Active Power Filter with Load Voltage Support Considering Current Harmonic Compensation, Applied Sciences, vol. 10, 1164 (2020), DOI: 10.3390/app10051664.
- [6] El-Hosainy A., Hamed H.A., Azazi H.Z., Elkholy., A Review of Multilevel Inverter Topologies, Control Techniques, and Applications, Nineteenth International Middle East Power Systems Conference (MEPCON), pp. 1265–1275 (2017), DOI: 10.1109/MEPCON.2017.8301344.
- [7] Demirdelen T., Inci M., Tumay M., Comparison of Three, Five and Seven Levels Diode Clamped Multilevel Inverter Topologies based Shunt Hybrid Active Power Filter for Harmonics Compensation with Equal DC Link, International Journal of Applied Mathematics, Electronics and Computers, vol. 4, no. 1, pp. 24–30 (2016), DOI: 10.18100/ijamec.83268.
- [8] Defay F., Llor A.M., Fadel M., Direct Control Strategy for a Four-Level Three- Phase Flying-Capacitor Inverter, IEEE Transactions on Industrial Electronics, vol. 75, no. 7, pp. 2240–2248 (2010), DOI: 10.1109/TIE.2009.2039457.

- [9] Rouabah B., Toubakh H., Djemai M., Ben Brahim L., Ghandour R., Fault Diagnosis Based Machine Learning and Fault Tolerant Control of Multicellular Converter Used in Photovoltaic Water Pumping System, Engineering, Environmental Science, vol. 11 (2023), DOI: 10.1109/access.2023.3266522.
- [10] Antoniewicz K., Rafal K., Model predictive current control method for four-leg three-level converter operating as shunt active power filter and grid connected inverter, Bulletin of the Polish Academy of Sciences, Technical Sciences, vol. 65, no. 5, pp. 601–607 (2017), DOI: 10.1515/bpasts-2017-0065.
- [11] Rouabah B., Rahmani L., Toubakh H., Duviella E., *Adaptive and Exact Linearization Control of Multicellular Power Converter Based on Shunt Active Power Filter*, Journal of Control Automation and Electrical Systems, vol. 30, no. 2, pp. 1019–1029 (2017), DOI: 10.1007/s40313-019-00510-w.
- [12] Bouhafs A., Rouabah B., Kafi M.R., Louzene L., Self-adaptive fault-tolerant control strategy of shunt active power filter based on multicellular converter, Diagnostyka, vol. 24, no. 4 (2023), DOI: 10.29354/diag/175006.
- [13] Djerboub K., Allaoui T., Champenois G., Denai M., Habib C., Article Swarm Optimization Trained Artificial Neural Network to Control Shunt Active Power Filter Based on Multilevel Flying Capacitor Inverter, European Journal of Electrical Engineering, vol. 22, no. 3, pp. 199–207 (2020), DOI: 10.18280/ejee.220301.
- [14] Othman S., Alali M.A., Sbita L., Barbot J.P., Ghanes M., Modeling and Control Design Based on Petri Nets Tool for a Serial Three-Phase Five-Level Multicellular Inverter Used as a Shunt Active Power Filter, Energies, vol. 17, pp. 5335 (2021), DOI: 10.3390/en14175335.
- [15] Taghzaoui C., Abouloifa A., Tighazouane B., Elallali A., Lachkar I., Mchaouar Y., Giri F., Advanced control of single phase Shunt Active Power Filter based on Flying Capacitor converter, IFAC Papers Online, vol. 55, no. 12, pp. 55–60 (2022), DOI: 10.1016/j.ifacol.2022.07.288.
- [16] Cortajarena J.A., Barambones O., Alkorta P., Cortajarena J., *Sliding mode control of an active power filter with photovoltaic maximum power tracking*, Electrical Power and Energy Systems, vol. 110, pp. 747–758 (2019), DOI: 10.1016/j.ijepes.2019.03.070.
- [17] Cibiraj N., Aratharajan M.V., Chattering reduction in sliding mode control of quadcopters using neural networks, VIT University, Chennai Campus, 1st International Conference on Power Engineering, Computing and Control, Energy Procedia, vol. 117, pp. 885–892 (2017), DOI: 10.1016/j.egypro.2017.05.207.
- [18] Furat M., Eker I., *Chattering eliminated adaptive sliding-mode control: an experimental comparison study*, Turkish Journal of Electrical Engineering & Computer Sciences, vol. 24, no. 2, pp. 605–620 (2016), DOI: 10.3906/elk-1309-137.
- [19] Djilali L., Sanchez E.N., Belkheiri M., First and High Order Sliding Mode Control of a DFIG-Based Wind Turbine, Electric Power Components and Systems, vol. 48, pp. 105–116 (2020), DOI: 10.1080/15325008.2020.1758836.
- [20] Benbouhenni H., Bizon N., Colak I., Thounthong P., Takorabet N., Simplified Super Twisting Sliding Mode Approaches of the Double-Powered Induction Generator-Based Multi-Rotor Wind Turbine System, Sustainability, vol. 14, no. 9, pp. 5014 (2022), DOI: 10.3390/su14095014.
- [21] Maharof M., Jamaludin Z., Mohammad S., Rashid A., Ahmed S., Abdullah L., *Super-twisting sliding mode controller for precise ball screw driven xy position milling table*, Journal of Advanced Manufacturing Technology, vol. 18, no. 3 (2024).
- [22] Din S.U., Rehman F.U., Khan Q., Smooth super-twisting sliding mode control for the class of underactuated systems, PLOS One, vol. 13, no. 10, e0203667 (2018), DOI: 10.1371/journal.pone.0203667.
- [23] Bey H., Krim F., Gherouat O., FPGA-Based Hardware in the Loop of Optimized Synergetic Controller for Active Power Filter, International Transactions on Electrical Energy Systems, vol. 1 (2023), DOI: 10.1155/2023/5810353.

- [24] Cortajarena J.A., Barambones O., Alkorta P., Cortajarena J., *Sliding mode control of an active power filter with photovoltaic maximum power tracking*, Electrical Power and Energy Systems, vol. 110, pp. 747–758 (2019), DOI: 10.1016/j.ijepes.2019.03.070.
- [25] Mahboub M.A., Roubah B., Kafi M.R., Toubakh H., *Health management using fault detection and fault tolerant control of Multicellular Converter applied in move electric aircraft system*, Diagostyka, vol. 3, no. 2, pp. 2449–5220 (2022), DOI: 10.29354/diag/151039.
- [26] Imam A.A., Kumar R.S., Al-Turki Y.A., Modeling and Simulation of a PI Controlled Shunt Active Power Filter for Power Quality Enhancement Based on P-Q Theory, Electronics, vol. 9, no. 4, 637 (2020), DOI: 10.3390/electronics9040637.
- [27] Ramirez J., Castro A., Zuniga P., Alanis A.Y., High Order Sliding Mode Control for Shunt Active Power Filter, IEEE International Autumn Meeting on Power, Electronics and Computing (ROPEC), Ixtapa, Mexico, pp. 26–50 (2016), DOI: 10.1109/ROPEC.2015.7395111.
- [28] Ghias M.Y.M., Pou J., Ciobotaru M., Agelidis V.G., Voltage-Balancing Method Using Phase-Shifted PWM for the Flying Capacitor Multilevel Converter, IEEE Transactions on power electronics, vol. 29, no. 9, pp. 4521–4531 (2014), DOI: 10.1109/TIE.2014.2320216.
- [29] Hemici K., Mahmoudi M.O., Bokhtache A.A., Zegaoui A., Aillerie M., Three-phases Flying-Capacitor Multilevel Inverter with Proportional Natural PWM Control, Energy Procedia, vol. 74, pp. 1061–1070 (2015), DOI: 10.1016/j.egypro.2015.07.744.
- [30] Farhi S.E., Sakri D., Goléa N., High-performance induction motor drive based on adaptive super-twisting sliding mode control approach, Archives of Electrical Engineering, vol. 71, no. 1, pp. 245–263 (2022), DOI: 10.24425/aee.2022.140208.
- [31] Feng Z., Fei J., Design and analysis of adaptive Super-Twisting sliding mode control for a microgyroscope, PLoS ONE, vol. 13, no. 1 (2018), DOI: 10.1371/journal.pone.0189457.
- [32] Belabbas B., Allaoui T., Tadjine M., Denai M., Comparative study of back-stepping controller and super twisting sliding mode controller for indirect power control of wind generator, International Journal of System Assurance Engineering and Management, vol. 10, pp. 1555–1566 (2019), DOI: 10.1007/s13198-019-00905-7.
- [33] Ouchen S., Benbouzid M., Blaabjerg F., Betka A., Steinhart H., *Direct Power Control of Shunt Active Power Filter using Space Vector Modulation based on Super Twisting Sliding Mode Control*, IEEE Journal of Emerging and Selected Topics in Power Electronics, vol. 9, no. 3, pp. 3243–3253 (2021), DOI: 10.1109/JESTPE.2020.3007900.